Plasmonics (2012) 7:665–675
DOI 10.1007/s11468-012-9357-1

Tuning the Propagation Constant by the Anticrossing Bandgap Prism Coupling Technique

Raquel Chuliá-Jordán · David Santamaría-Pérez

Received: 20 September 2011 / Accepted: 16 March 2012 / Published online: 13 April 2012

Abstract A novel plasmonic structure based on an anticrossing bandgap prism coupling technique is proposed. The study has been carried out using photonic crystals based on diffraction gratings (bounded by dielectrics with identical dielectric functions) together with a high refractive index prism to couple the long-range surface plasmon polaritons to photons. We analyse the structure and demonstrate the ability for tuning the propagation constants of plasmon modes by changing the thickness of the gold grating. The comparison to non-bandgap techniques is studied, and the influence of the plasmonic configuration on the plasmon propagation constant is discussed as well. Experimental measurements were also carried out to confirm the validity of our model.

Keywords Anticrossing bandgap · Diffraction gratings · Gold thickness dependence · Propagation constant · Prism coupling technique · Long-range surface plasmon polaritons

Introduction

Interest in photonic materials has increased over the last years due to the potential they offer to control the optical properties of materials, such as plasmonic bandgap lasers [1], amongst others. In essence, photonic crystals consist of regularly repeating internal regions of low and high dielectric function, which influence the propagation of electromagnetic (EM) waves. A corrugated metallic surface may be used to provide the appropriate periodicity of the photonic crystal structure, which must be of the same length scale as half the wavelength of the EM waves, to result in an energy bandgap in the propagation of the surface plasmon polaritons (SPPs) modes. Barnes et al. [2], for instance, presented an analytic model to describe the existence of photonic energy gaps in the propagation of surface plasmon polaritons on corrugated surfaces.

For thin metal layers (<100 nm) embedded by dielectrics with identical dielectric functions, the single interface SPPs on the two interfaces are degenerated and will interfere with each other to form two coupled SPPs, described as the short-range SPPs (SRSPPs) and the long-range SPPs (LRSPPs). Thus, at the same in-plane momentum, two coupled SPPs modes of different frequencies are formed, which are distinguished by having different surface charge-density distributions [3, 4].

Sarid [5] was the first one to report theoretically that, in case of a flat thin metal slab, there is a metal thickness dependence of the difference between the real (effective refractive index) and the imaginary (attenuation) propagation constant components of the LRSPPs and the SRSPPs. Besides, Hooper and Sambles [4] and Chen et al. [3] investigated the effect of coupled SPPs (the LRSPPs and SRSPPs) on the optical response of a thin metal film conformally and nonconformally corrugated on both surfaces and bounded by dielectrics with identical dielectric functions. They found that a small additional first harmonic component, $2K_g$ (where K_g is the grating vector), to the grating shape of a conformally corrugated structure causes

R. Chuliá-Jordán
Max Planck Institute for Polymer Research,
Ackermannweg 10,
Mainz 55128, Germany

R. Chuliá-Jordán (✉) · D. Santamaría-Pérez
Departamento de Química-Física I,
Universidad Complutense de Madrid,
Avda. Complutense s/n,
Madrid 28040, Spain
e-mail: rchulia@pas.ucm.es

an anticrossing behaviour where the LRSPPs and the SRSPPs should cross in the dispersion curves. With increasing slab thickness, this anticrossing behaviour becomes the same as the bandgaps observed on single interface gratings.

Although different techniques for surface plasmon resonance excitation have been applied [6, 7], they have focused on improving sensitivity and evanescent field enhancement by optimization of the thickness of the metal film [8], whereas optimization in terms of the propagation constant has not been done so far. This will be the aim of this work. To this end, we use a new four-mode anticrossing bandgap plasmonic structure [9], which will allow tuning the propagation constant of both anticrossing modes, the long- and short-range surface plasmons by changing the metal thickness.

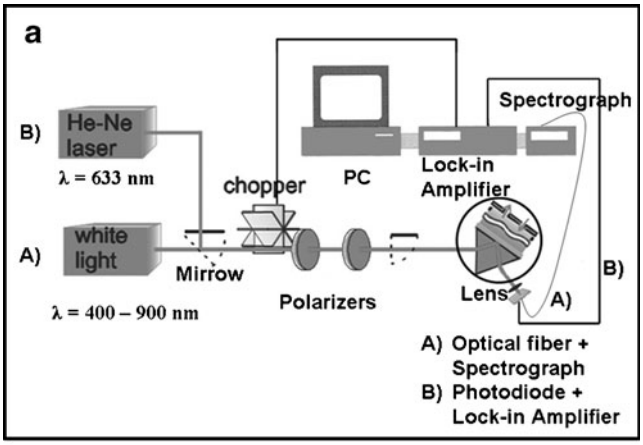

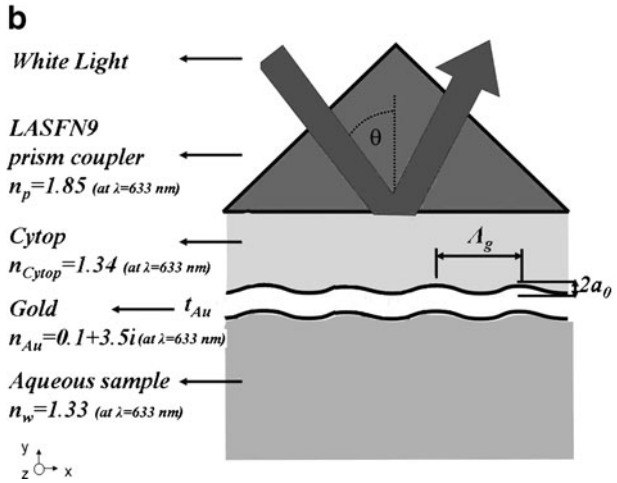

Fig. 1 **a** Schematic diagram of the optical setup used in this study. **b** Geometry of the bandgap prism coupling technique. This is based on a prism coupler to resonantly excite LRSPPs and SRSPPs propagating along optically symmetric thin metal conformal replica grating. It also included the coordinate system, the polar angle θ, the grating pitch Λ_g and the thickness of the gold layer t_{Au}. The Cytop and the aqueous solution form the refractive index symmetrical structure needed for the excitation of LRSPPs. In the experiments, an index matching fluid is used between the *LASFN9* prism and the substrate of the replicated metal grating

Methods and Materials

To open a plasmonic bandgap, there must be standing waves of surface plasmons, which require interaction between forward and backward propagating plasmons. In our case, this is produced by thin metal diffraction gratings (bounded by dielectrics with identical dielectric functions) that do not have a $2K_g$ component but a high refractive index prism to couple photons to the LR- and SRSPPs modes (the so-called bandgap prism coupling technique). Since the fundamental component, K_g, of the grating is not used to couple light in and out of the sample, it may now be used to produce the gap [9]. This method allows a significantly stronger coupling between the LR- and SRSPPs modes and photons than the double grating technique. Note that the double grating technique is limited to $2K_g a_1 \approx 0.06$ for the case of SPs [2], whereas the $K_g a_0$ used in this work is 0.093 (a_1 and a_0 being the first-order and the fundamental harmonic amplitudes, respectively).

Geometry of the System

The optical setup and the geometry used in this study are depicted in Fig. 1a, b, respectively. The geometry forms an optically symmetric metal replica grating with respect to the refractive index of the Cytop–water medium, needed for the excitation of LRSPPs. Note that the refractive index of the Cytop buffer layer (Cytop from Asahi Inc., Japan, with n_{Cytop}=1.34 at λ=633 nm) matches that of aqueous samples (refractive index of water n_w=1.33 at λ=633 nm). The refractive index of the cover material (prism) is n_P=1.85 at λ=633 nm. Gold was our material of choice for the thin metallic film deposited on the sensor surface as it is little affected by oxidation and it provides high sensitivity. The dielectric function was obtained from Palik's handbook of optical constants of solids (n_{Au}=0.1+3.5i) [10]. In the case of gold, interband effects already start to occur for energies in excess of 1 eV. The main consequence of these processes concerning surface plasmon polaritons is an increased damping and a competition between the two excitations at visible frequencies [11]. We have chosen the coordinate system such that the z-axis is in the direction of the grooves and that the y-axis is orthogonal to the plane of the grooves. The width of the grooves in x direction is the periodicity Λ_g of the grating. The profile describing the thin metal replica grating is given by $[y_1(x)=a_0 \sin(K_g x)]$ for the lower metal–water interface and $[y_2(x)=a_0 \sin(K_g x)+t_{Au}]$ for the upper metal–Cytop interface, where t_{Au} is the mean gold thickness between the two surfaces (ranging from 10 to 120 nm), Λ_g= 254 nm is the grating pitch, a_0 is the fundamental harmonic

amplitude of the K_g component (a_0=7.5 or 10 nm), and K_g= $2\pi/\Lambda_g$ the grating vector, which runs parallel to the x-axis. We suppose that a plane wave is incident from above with a direction located in the x–y plane (i.e. in the plane perpendicular to the grooves) and under the incident angle θ. The wavelength of the light in air is λ, and we consider the case of transverse magnetic (TM) polarized radiation incident at the fixed azimuth angle of φ=0°, where the vector of the magnetic field H shows in the direction of the grooves, i.e. in the direction of the z-axis.

Theoretical Simulations

To solve the classical TM case, we have used a finite element program [12]. The unbounded domain is treated by coupling with boundary element methods. The z component of the incident magnetic field H_z^{incident} used in this code is normalized and guarantees that the incident light wave has a fixed intensity (length of Poynting vector) independent of the cover material. The values of the efficiencies and phase shifts of the reflected and transmitted plane wave modes are independent of this scaling. Only the Rayleigh coefficients depend on this normalization factor. The z component of the complete field H_z satisfies the Helmholtz equation in any domain of the cross-section plane with constant materials.

Grating Synthesis (Fabrication)

The samples studied experimentally were metal gratings on silicon–wafer substrates (CrysTec) fabricated in a clean room (class 100 type). The gratings were made by first covering a silicon wafer with the primer silane (Microposit UN 2924, Shipley, Rohm and Haas electronic materials) to improve its photo-resistance adhesion. After 30 s, the sample was spin-coated for 1 min at 4,000 rpm to remove the excess of primer solution. Immediately afterwards, the photoresist was spin-coated on top of the primer (also 1 min at 4,000 rpm). This photoresist was diluted with an equal volume of Microposit EC-solvent to reduce the viscosity. An approximately 170-μm-thick layer of photoresist was deposited. The spin-coated substrates were heated to a temperature of 95 °C for 30 min in a vacuum oven (soft baking) to remove the remaining solvent. After that, the photoresist part of the spin-coated substrates were exposed to two coherent expanded interfering HeCd laser beams (λ=441.6 nm, 40 mW, 4270 NB helium–cadmium laser, LiCONix, Melles Griot Inc.), interfering in the plane of the resist layer. After drying the developed samples in the oven at a temperature of 110 °C for 90 min, the surface corrugation of the resulting developed samples was transferred into the silicon wafer by reactive ion etching with a mixture of CF_4 and O_2 in a high vacuum chamber. The resulting gratings on silicon wafer were cleaned with acetone. The grating profile was characterised with an atomic force microscope, being the shape of the profile obtained purely sinusoidal [9]. These master gratings were replicated to obtain identical samples, i.e. with the same grating constant and depth. For this purpose, a layer of gold was evaporated onto the surface of the master gratings. Spin-coated Cytop was onto the evaporated side, and a thickness of 1,000 nm was fixed. The lower part of this Cytop film acquires the shape of the grating whereas the upper part is flat. To remove the remaining solvent in the Cytop, the samples were gently heated. The coated flat side of the Cytop's film was glued (Epotec 377, Polytec) on a cleaned glass slide, which was made of high refractive index LASNF9-glass (n_{LASNF9}=1.85 at λ=633 nm, Schott Glass GmbH), with a size of 25×25×1 mm^3. Again the samples were placed in a vacuum oven. The removal of the silicon wafer (master grating) leaves a gold replica grating on the Cytop glued to the glass substrate. In the experiments reported here, we used the replicas of the etched samples which had a low roughness due to the stripping process. The sinusoidal replica gratings had a Λ_g of 254 nm, a grooved depth ($2a_0$) of 15 and 20 nm and a gold thickness (t_{Au}) of 40 nm.

Results and Discussion

In reflection, the single diffracted SPPs modes of a metal grating are shown as reflectivity minima in the zero-order beam, since the re-radiated light is in anti-phase with the specularly reflected light [13]. If the metal grating film embedded by dielectrics with identical dielectric functions is thin enough (less than 100 nm for light in visible and near infrared part of spectrum), the evanescent wave penetrates through the metal film and couples with a surface plasmon at the outer boundary of the metal film (LR- and SRSPPs). Because of the attenuation through the film, any re-radiated SPP light scattering from the second surface is much weaker than that re-radiated from the first surface, and so both the SR- and LRSPPs are still seen as reflectivity minima. Hence, by measuring the reflectivity data as a function of wavelength (600 nm≤λ_0≤925 nm) at various fixed polar angles (41°≤θ≤52°) and noting all the reflectivity minima, the wavelength-angle dispersion curves of the SPPs modes associated with the structure for TM polarized radiation incident at φ=0° are obtained. The plasmons on each interface of the thin metal film are not separately excited, and therefore, the observed dispersion relation does not depend on the illuminated interface.

Simulations

The propagation constants of plasmon modes of the considered structure can be found from the dispersion relation curves. Hence, we simulate the dispersion curves of the

LR- and SRSPPs of our system for different slab thickness ranging between 10 and 120 nm and an amplitude of 7.5 nm. This is shown in Fig. 2 where the wavelength—polar angle dispersion curves for slab thickness of 20 nm (a), 40 nm (b) and 60 nm (c) are given.

In Fig. 2c, a total of four different modes can be identified. The two approximately vertical branches are due to the prism that couples the photons to the thin metal slab plasmons and

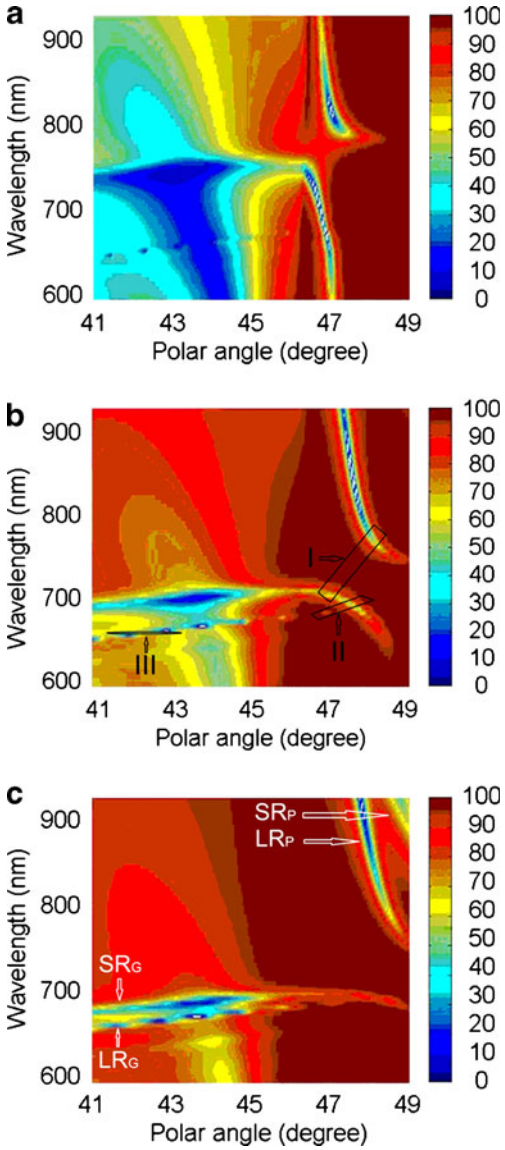

Fig. 2 The simulated optical response as a function of wavelength (nanometres) and polar angle θ (degrees) on a conformal, sinusoidal corrugated, thin gold grating slab of 7.5 nm fundamental harmonic amplitude and 254 nm pitch, embedded by dielectrics with identical dielectric functions and in the Kretschmann configuration. Results of three different thicknesses are plotted: **a** 20 nm, **b** 40 nm and **c** 60 nm. **b** The different crossing points of plasmon modes are denoted as *I* SR_G–LR_P intermode bandgap, *II* SR_G–LR_G crossing point and *III* small gaps in the LR_G branch caused by diffraction from the higher-order Fourier components. **c** The notation of the different assigned modes is included

are denoted with the subscript P [9]. As mentioned above, the gold slab was thin enough for the surface plasmons on both interfaces to interact, resulting in two modes: The one on the right side is the SR_P and the one on the left side the LR_P (see Fig.2c). On the other hand, due to the corrugation of the thinner gold gratings (subscript G), two approximately horizontal modes are also obtained [9]. The upper one is the SR_G and the lower one the LR_G. The assignment of the different modes has been done using both their frequencies (energies) and widths. The prism and grating modes were differentiated according to recent simulations in this system for a flat metal slab [9]. The LR and SR modes, on the other hand, were assigned according recent experiments on a prism–grating system [3]. The higher-frequency mode corresponds to the LRSPP, whereas the lower-frequency mode corresponds to the SRSPP [3]. Additionally, the widths of the modes verify the good assignment of the LR and SR modes, i.e. the sharper resonance corresponds to the LR mode.

At first sight, we can observe in Fig. 2 that, for a fixed gold thickness, the wavelength values of the SR_G branch initially increase with the incident polar angle (group velocity, $v_g<0$). At the LR_P–SR_G anticrossing point, the v_g becomes zero ($v_g=0$), and subsequently, after the LR_P–SR_G coupling, the wavelength decreases ($v_g>0$). Hence, the SR_G wavepacket accelerates. On the other side, for a fixed gold thickness, the LR_P group velocity decreases until it reaches a uniform motion after the LR_P–SR_G coupling.

In the dispersion maps of Fig. 2, there are different crossing points of plasmon modes. Whether there is a bandgap at each crossing point and its behaviour depends on the film structure and therefore on the metal thickness. The biggest bandgap observed for all of the gold thicknesses corresponds to the anticrossing point ($k_x\neq0$) of the LR_P mode and the SR_G mode (denoted as "I" in Fig. 2b). This interaction originates an *intermode* bandgap because of the interaction between the forward and backward propagating plasmon. On one side, the prism coupler is used to resonantly excite LR_P modes propagating along the metal film at $\Re\{\beta_P\} = \frac{2\pi}{\lambda} n_P \sin\theta$, where β is the propagation constant. On the other side, as the metal film is corrugated with a period Λ_g, these modes cannot be excited at wavelengths where the propagation constant of the SR_G modes fulfil the Bragg-scattering condition: $2\Re\{\beta_G(\lambda)\} = \frac{2\pi}{\Lambda_g}$. In this case, the LR_P will be the upper anticrossing bandgap branch and the SR_G the lower anticrossing bandgap branch.

Another phenomenon that can be observed is the change in the direction of the SR_G branch when the LR_G mode interacts with it (crossing point named as "II" in Fig. 2b). This fact will be analysed and discussed in the next section.

Additionally, very small gaps in the LR_G branch caused by diffraction from the higher-order Fourier components of the grating profile are observed (denoted as "III" in Fig. 2b).

These very small plasmonic bandgaps appear for gratings that have no $2K_g$ components and no prism is used, regardless of the relative phase of the gratings on each interface. They are originated at least through two diffraction processes. Although these processes are quite weak, these bandgaps (III) are smaller in wavelength units than the biggest bandgap (I), indicating stronger cross coupling between the modes [1, 14].

Experiments

The aim of our experiments is to measure the dispersion curve of our system, thus allowing the experimental results to be compared to those found in the numerical simulations. We have carried out a series of detailed experiments to precisely determine the dependence of the LR- and SRSPPs propagation, at normal incidence to the grooves, upon the gold thickness of the grating, t_{Au}=40 nm. The incidence angle for the experimental case must be corrected if we want to compare both dispersion curves properly. This is due to the fact that the incidence angle in the simulations corresponds to that at the prism–Cytop dielectric interface while in experiments is that at the air–prism interface. After this correction, the dispersion curve shown in Fig. 3a is obtained. Experimental results are in good agreement with those from our simulations (see Fig. 3b), verifying the validity of our model for gratings with a pitch of 254 nm, a grooved depth ($2a_0$) of 20 nm and a gold thickness (t_{Au}) of 40 nm. Hence, it proves that our code is suitable when applied to this specific problem.

SR_G (Lower Anticrossing Bandgap Branch) and LR_G Branches

Now we will focus on the analysis of the anticrossing interaction "I" between the LR_P and the SR_G and the crossing interaction "II" between the LR_G and the SR_G modes of the simulated wavelength-angle dispersion curves for different slab thicknesses. Our results will be compared to the cases of systems with either only a prism (superscript P, see Fig. 6b) or only a grating (superscript G, see Fig. 4b), where no anticrossing bandgap is possible.

To understand the anticrossing interaction, it is useful to investigate separately the dispersion curves of the modes involved. Firstly, we will focus on the wavelength-angle behaviour of the lower anticrossing bandgap branch, SR_G, as a function of the gold thickness (see Fig. 4a). Note that this branch can be divided into three different sections: on one hand, the part of the SR_G curves at lower angles (approximately horizontal) that is not affected by the LR_P and which follows a phonon-like behaviour and on the other hand, the other two parts of the SR_G curves on the right (angles higher than the total reflection angle θ_{iL}=arcsin

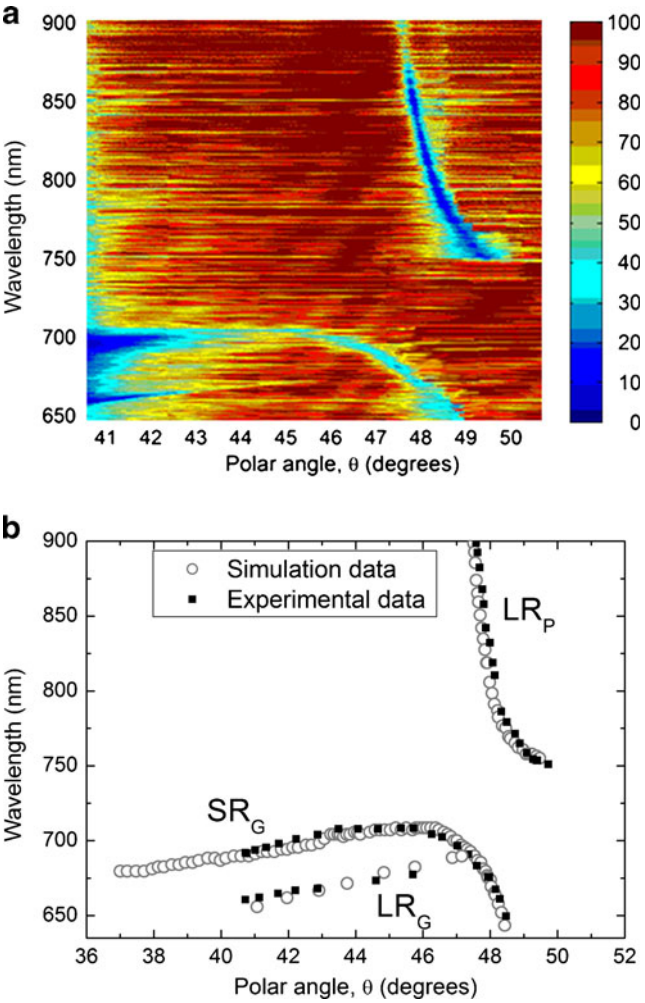

Fig. 3 **a** The experimental optical response of the system: Λ_g=254 nm, a_0=10 nm, t_{Au}=40 nm (*solid squares*). This response is in good agreement with numerical simulations (*empty circles*) of the LR_P and the SR_G curves on a conformally corrugated thin metal slab with the same parameters using the bandgap prism coupling technique (**b**)

(n_{Cytop}/n_{prism})=46.4° approximately) that can be affected by the LR_P (anticrossing point "I") and LR_G (crossing point "II"), respectively, and which follows a photon-like behaviour. These regions will be denoted as 1, 2 and 3 as indicated in Fig. 4a.

To analyse the effect of the gold thickness on the behaviour of the SR_G curves, we have considered that each of the three regions mentioned above can be fitted to a straight line with slope: $m(t_{Au}) = \frac{d\lambda}{d\theta}$. The variation of m with thickness t_{Au} is plotted in Fig. 5 and points out that m can be fitted to a potential-type equation: $m \propto t_{Au}^{b}$, where b=1, −2.51 and −2.86 for the first, second and third sections, respectively, and t_{Au}>20 nm:

1. Analysing the effect of the gold thickness in the first region, for angles below θ_{iL}=46.4° (exception at t_{Au}= 10 nm), we observed that the SR_G curves have similar

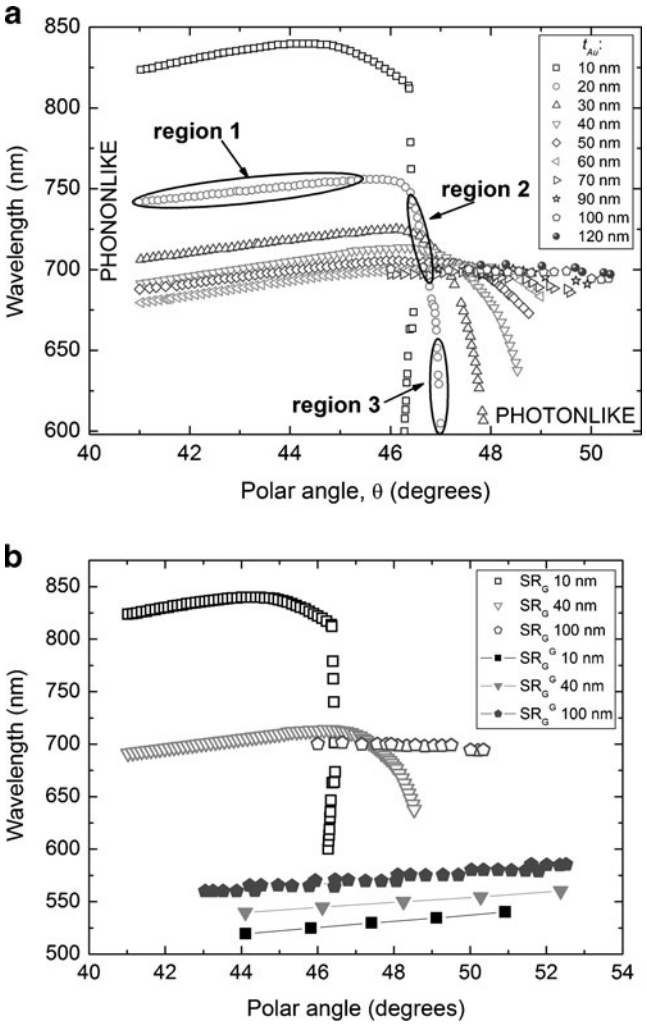

Fig. 4 **a** Wavelength-angle curves of the lower anticrossing bandgap branch, SR_G, as a function of the gold thickness. **b** Comparison between the behaviour of SR_G at the two different structures: prism + grating (*without superscript*, *empty symbols*) and only grating (*superscript G*, *solid symbols*)

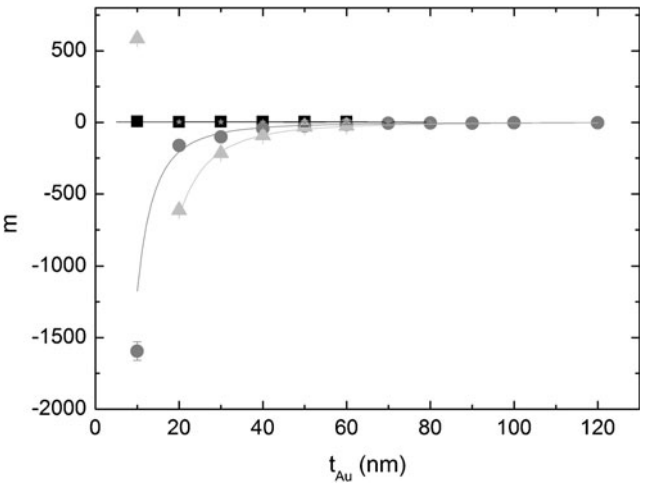

Fig. 5 Slopes of the three different regions of the SR_G curves as a function of the gold thickness. Regions: 1 (*solid squares*), 2 (*solid circles*) and 3 (*solid triangles*). For the case of SR_G^G, the slopes are similar to those of region 1 and, consequently, *symbols* are superposed. *Superscript G* is associated to the configuration in which only a grating and no prism is used

slopes $m_1(t_{Au}) = (d\lambda/d\theta)_1 \propto 0.027 \cdot t_{Au}(\text{nm})$, which are almost independent on the thickness of the gold. This slope is also similar to those of the LR_G mode (at every polar angle) of our system and the SR_G^G mode (at every polar angle) excited in a system only formed by a grating without a prism (see Fig. 4b). This is due to the fact that the angle at this region is smaller than the critical angle (θ<46.4°), and therefore, no LR_P modes can be excited. The propagation constant will remain almost constant by changing the gold thickness. Moreover, for a fixed incidence angle, the SR_G goes to lower wavelengths as the gold thickness increases. For t_{Au}=100 nm, the λ values in "region 1" using our system are about 130 nm higher than in the only-grating configuration. On the top of that, the wavelength values change as much as 300 nm in the case of t_{Au}=10 nm. Therefore, the combination of prism plus grating, compared to a system which it is only formed by a grating, increases the wavelength of the SR_G from 19 % up to almost 38 %.

The propagation constant of plasmon at the Cytop–gold interface is the same for both structures. Here, it is important to remark that both plasmonic structures are not using the same element to couple the light to the plasmon. In the case of the only-grating configuration, it is the grating the responsible to fulfil the phase matching condition whereas, in our configuration, is the high refractive index prism ($n_{prism} > n_{Cytop}$) the responsible to increase the propagation constant of the photons. Hence, the refractive index involved in the coupling in the four-mode plasmonic structure is higher than that of the only-grating configuration. Since the propagation constant is proportional to the refractive index and inversely proportional to the wavelength and that the propagation constant of the photons must reach the same propagation constant of the plasmon propagating at the Cytop–gold interface, we can understand that the use of a high refractive index prism implies an increase of the incident light wavelength used for the coupling, compared to that in the only-grating configuration.

2. For incident angles larger than θ_{iL}=46.4, the SR_G presents a new-linear photon-like behaviour which depends on the gold thickness $\left(m_2 = (d\lambda/d\theta)_2 \propto t_{Au}^{-2.51}\right)$. The difference with the previous behaviour is a consequence of the coupling between the SR_G and the LR_P branches, which is responsible of the anticrossing bandgap. This coupling becomes weaker as the t_{Au} increases since the coupling angle of the bandgap moves to higher values (see Fig. 8).

This can be also seen in Fig. 4a in which, by increasing t_{Au}, the slope of the "region 2" becomes closer to that of "region 1" because the bandgap does not affect the SR_G. A dramatic decrease of the propagation velocity is obtained as the t_{Au} is decreased.

3. The slope of the different curves changes once more due to the coupling between the SR_G branch and the LR_G branch (region 3). This new coupling is weaker than the SR_G–LR_P coupling and is also dependent on the gold thickness. The slopes of the SR_G curves after this second coupling are described by the following potential equation $\left(m_3 = (\mathrm{d}\lambda/\mathrm{d}\theta)_3 \propto t_{Au}^{-2.86}\right)$.

In "region 2" and "region 3," at a fixed gold thickness, the lower anticrossing bandgap branch, SR_G, moves to smaller wavelengths as the angle increases. This is the opposite behaviour of that observed for angles smaller than 46°. An exception is obtained at 10 nm gold thickness, in which the anticrossing bandgap branch in "region 3" shows a positive $\lambda(\theta)$ slope. At a fixed wavelength, the SR_G goes to bigger incidence angles as the gold thickness increases. As the amount of the shift increases with increasing amplitude of the grating surface, the phase velocity of the SR_G oscillations slows down.

As a general behaviour, it can be said that the LR_G branch follows a linear behaviour over the whole range of angles studied independently on the thickness of the gold (see Fig. 2). This is due to the fact that, in our particular system, the LR_G will not coupled to any prism mode, and therefore, its propagation constant will not be affected by the change of gold thickness. At a fixed gold thickness, the LR_G branch goes to higher wavelengths as the angle increases, like the SR_G for $\theta < \theta_{iL}$ (same slope). Moreover, the LR_G and the SR_G modes approach each other in wavelength as the grating thickness increases, becoming a unique branch (surface plasmon, SP_G) for $t_{Au} > 110$ nm. Hence, the gold's thickness allows to control the distance between both curves (LR_G and SR_G). On top of that, the two modes move at a different rate: (a) the upper SR_G branch moves to lower λ faster than the lower LR_G branch moves to higher wavelengths, as the t_{Au} increases. The lower branch (LR_G) moves only slightly to higher wavelengths, being almost independent on the gold's thickness. As mentioned above, this is due to the fact that in our particular system, the LR_G is not coupled to any prism mode, and therefore, its propagation constant is not affected by the change of gold thickness.

LR_P (Upper Anticrossing Bandgap Branch) and SR_P Branches

Now we will focus on the wavelength-angle behaviour of the upper anticrossing bandgap branch, LR_P, as a function of the gold thickness (see Fig. 6a). In order to analyse the effect of our four-mode plasmonic structure on the LR_P mode, we will compare our results to those obtained in a system with only a prism (absence of a bandgap). The wavelength-angle curves corresponding to the LR_P can be defined by an exponential decay function $\lambda^{LR_P}(\mathrm{nm}) = \lambda_\infty + \exp(A - B \cdot \theta)$, where B is the so-called decay constant. It is important to remind here that all the LR_P curves are located at incidence angles higher than the total reflection angle. The interaction between the LR_P branch and the SR_G causes the significant changes in their wavelength-angle curves in the range 46–51° and produces the anticrossing bandgap. These changes from photon-like to phonon-like behaviour are clearly dependent on the gold thickness and take place at smaller wavelengths and bigger incident angles for thicker gold gratings.

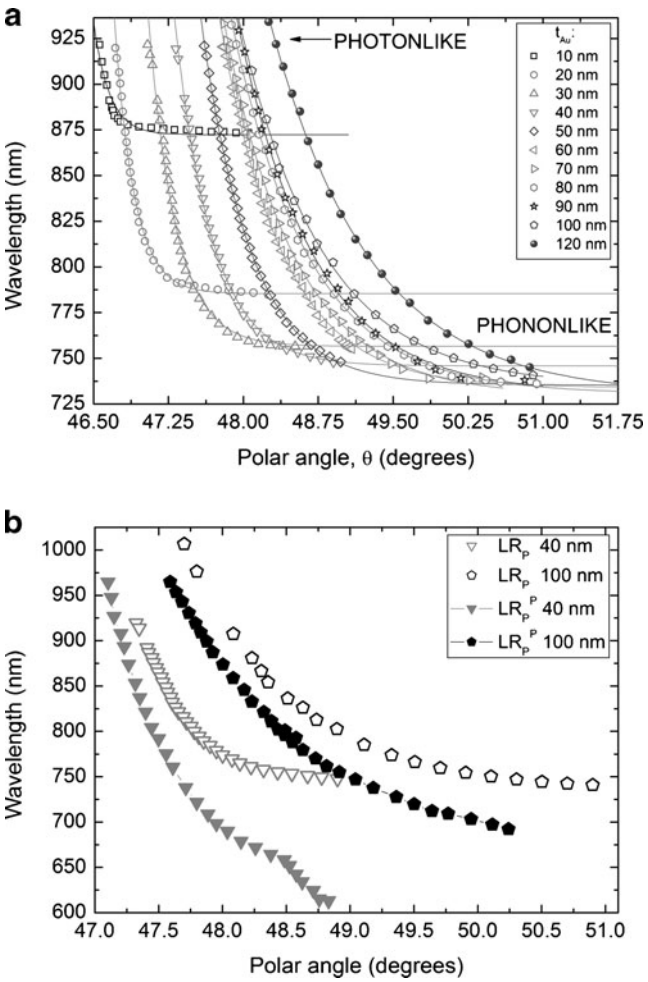

Fig. 6 **a** Wavelength-angle curves of the upper anticrossing bandgap branch, LR_P, as a function of the gold thickness. The curves have been fitted to an exponential decay function (*solid lines*) as defined in the text. The values of the fitted parameters λ_∞, A, B are collected in Table 1. **b** Comparison between the LR_P behaviour in two different configurations: prism + grating (*without superscript*, *empty symbols*) and only prism (*superscript P*, *solid symbols*)

We define λ_∞ (LR_P), by comparison with polaritons in crystal lattice, as the transverse optical phonon wavelength in the absence of coupling with photons. This corresponds to the minimum wavelength of the LR_P branch. λ_∞ (LR_P) is obtained by fitting to an exponential decay function the curves of Fig. 6. The thicker the grating is, the lower the value of λ_∞. All the fitted parameters (λ_∞, A, B) for different gold thicknesses are collected in Table 1. From these data, it can be inferred that λ_∞ decreases at a slower rate for thicker gratings. It is remarkable that this rate is approximately similar to that at which the SR_G moves down in wavelength as the t_{Au} is increased from 10 to 120 nm. For the sake of comparison, in Fig. 6b, we have represented the long-range mode of the prism $\left(LR_P^P\right)$ of a system consisting only of a prism, without a grating. Therefore, the combination of prism plus grating, compared to a system which is only formed by a prism, increases the wavelength of the LR_P.

The parameter, B, will allow evaluating the strength of the anticrossing coupling, providing some information about the "extra force" that acts on the LR_P wavepacket. The decay constant, B, of the upper LR_p anticrossing bandgap branch is represented in Fig. 7 as a function of the gold thickness. An increase of t_{Au} entails a decrease of B, which tends to 1. In the case of the LR_P wavepacket, it reaches a uniform motion after this coupling (I). However, note that in the case of the system consisting only of a prism, B^P increases for thinner gold gratings only down to t_{Au}= 30 nm, where B^P reaches its maximum value. Below this point, B^P falls abruptly to 1. The increase in B^P is due to the backbending [13], as it can be seen in Fig. 5b for 40 nm gold $\left(LR_P^P\right)$. Nevertheless, the increase of B in our system with decreasing the gold thickness is due to the presence of the bandgap. Since some wavelengths are no more allowed to propagate the LR_P mode, its group velocity increases to reach faster the uniform motion (v_g=0). Therefore, a stronger coupling is obtained for values larger than 1 ($B>1$). For t_{Au}<100 nm (region of LR_P modes), the decay constant is correlated with the gold thickness (see inset Fig. 7). The product $B \cdot t_{Au}$ gives a constant value for both cases (the bandgap and non-bandgap structures). However, although in both cases the LR_P goes to smaller wavelengths when the angle increases, as a consequence of the coupling between the LR_P and the SR_G in the bandgap structure, the correlation factor differs. Thus, in the bandgap case, $B \cdot t_{Au}$=104.7±1.7, whereas in that of the structure based only on a prism $B^P \cdot t_{Au}$= 79±2. The constant value of P + G configuration is therefore approximately 25 % larger as a consequence of the anticrossing coupling between the LR_P and the SR_G modes.

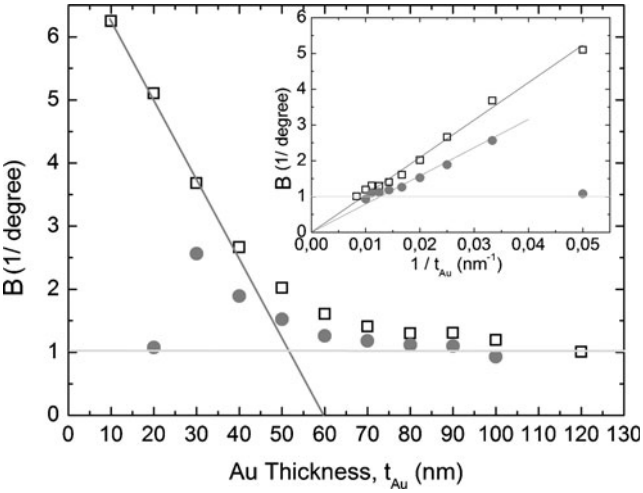

Fig. 7 Decay constant of the upper LR_p anticrossing bandgap branch as a function of the gold thickness. Comparison between the LR_P mode behaviour in two different configurations: prim + grating (*without superscript*, *empty squares*) and only prism (*superscript P*, *solid circles*). *Inset*: Correlation between the decay constant, B, and the gold thickness

Table 1 Fitted parameters in the exponential decay function that define the behaviour of wavelength-angle curves of the LR_P mode: λ_∞, A and the decay constant B, for different gold thicknesses

Gold thickness	λ_∞ (nm)	A	B
10 nm	872.4±0.9	297±2	6.30±0.8
20 nm	785.4±0.8	243±2	5.10±0.13
30 nm	756.6±0.7	178.4±1.5	3.7±0.2
40 nm	745.8±0.7	131.3±1.1	2.66±0.06
50 nm	735.4±0.7	101.4±0.9	2.020±0.033
60 nm	734.0±0.7	82.1±0.9	1.607±0.018
70 nm	729.7±1.2	72.7±1.1	1.409±0.024
80 nm	730.7±0.7	67.5±0.6	1.299±0.014
90 nm	731.1±0.8	67.995±0.006	1.307±0.022
100 nm	731.0±0.8	54.8±0.5	1.026±0.011
120 nm	730.0±0.8	53.8±0.3	1.006±0.015

Finally, we have determined the position of the anticrossing coupling point by calculating the bisection of the two straight lines that would define the LR_P branch behaviour at lower and higher incidence angles. Thus, the anticrossing coupling wavelength $\left(\lambda_{ACC}^{LR_P}\right)$ presents an exponential dependence on the gold thickness: $\lambda_{ACC}^{LR_P}(\text{nm}) = 731(4) + e^{5.746(3)-0.0826(2)\cdot t_{Au}}$.

The upper anticrossing LR_P^I coupling angle, on the other hand, follows a linear behaviour with t_{Au} as depicted in Fig. 8. The lower anticrossing SR_G^I data are also represented. Both dependencies are linear and have exactly the same correlation $\theta \propto 0.0440(8) \cdot t_{Au}$. The positions of the reflection minima displace to larger resonance angles θ with increasing t_{Au}. Therefore, the LR_P and SR_G phase velocities decrease with increasing gold thickness due to the multiple scattering. In Fig. 8, the SR_G^{II} coupling angle is also plotted. As it can be seen, it follows the same tendency as the LR_P^I and SR_G^I coupling angles.

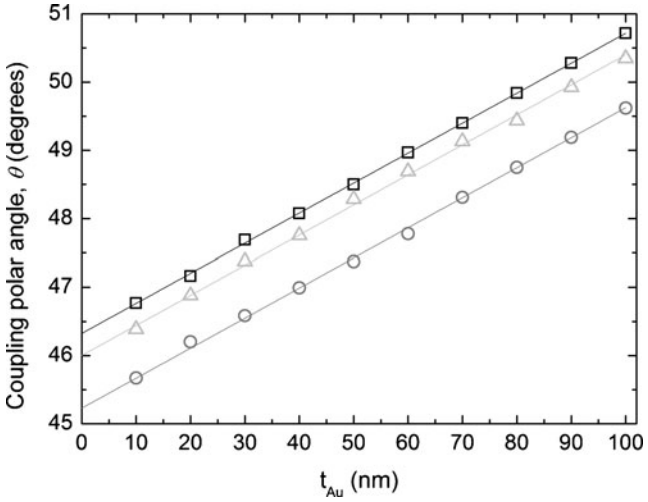

Fig. 8 Coupling angle versus gold thickness for LR_P^I (*empty squares*), SR_G^I (*empty circles*) and SR_G^{II} (*empty triangles*) branches. The *superscripts I* and *II* denote the different crossing points of plasmon modes (see Fig. 2b). All of them show the same correlation $\Theta/t_{Au}=0.044\pm 0.0008$

Another interesting point to highlight is the softening of the LR_P–SR_G coupling with gold thickness (see Fig. 2). This softening is also accompanied by a displacement to smaller wavelengths of the bandgap centre.

The SR_P branch, which can be observed in Fig. 2 (t_{Au}= 60 nm), moves to lower incident angles as the gold's thickness increases. This tendency is the opposite to that observed for the LR_P branch. Therefore, both branches (LR_P and SR_P) close each other and merge into a single SP_P branch at t_{Au}=120 nm. This thickness value is consistent with the t_{Au} value of the LR_P and SR_P merging.

Real Propagation Constants

To understand the characteristic features of the optically symmetric structure based on a four-mode anticrossing bandgap sensor, we have plotted in Fig. 9 the propagation constants of different modes in three different configurations as a function of the gold thickness. Thus, we can compare our data to those obtained using only either a prism or a grating, where no bandgap exists. The value of the propagation constants for the bandgap system (prism + grating) is always smaller than those using only a prism or only a grating. Consequently, the propagation constant curves of different systems never overlap or cross each other for a fixed polar angle (see Fig. 9a). The

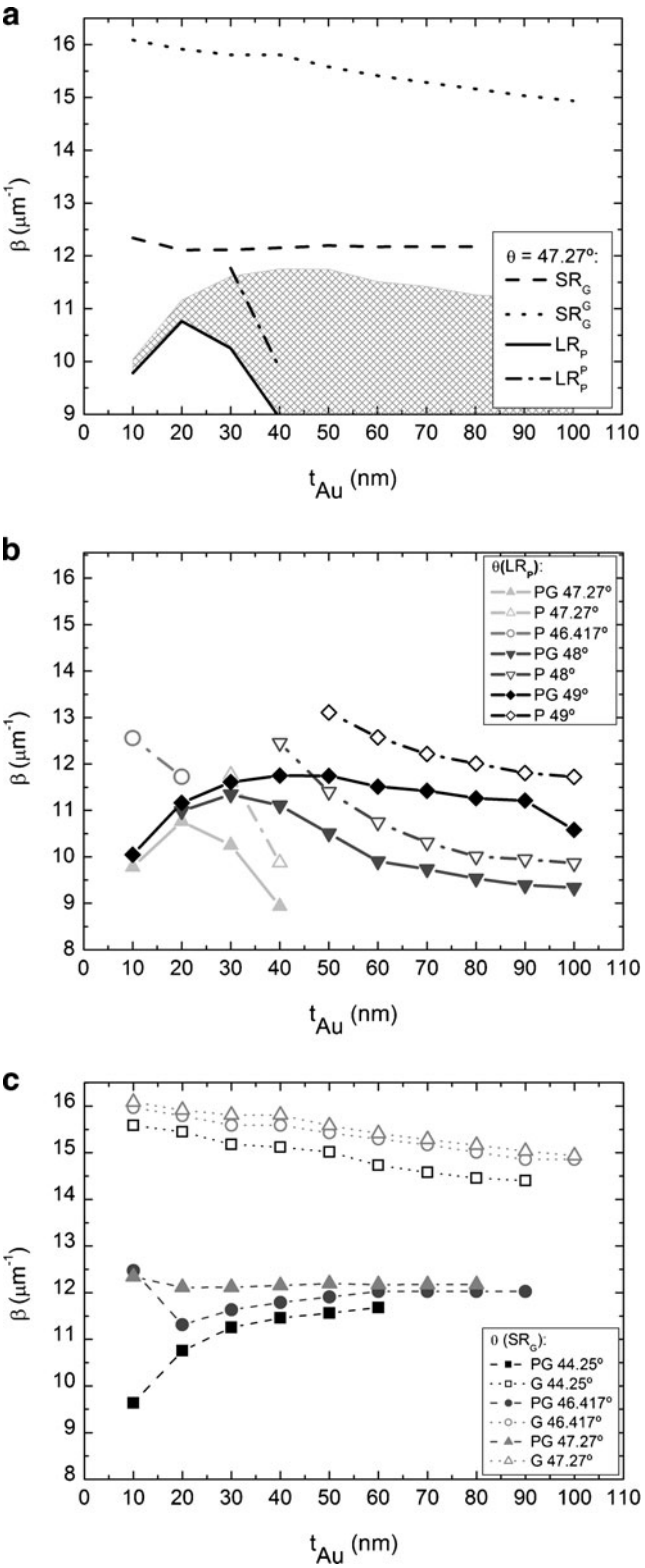

Fig. 9 **a** Propagation constants of the plasmon modes of the considered structures as a function of the gold thickness. The *solid* and *dashed curves* correspond to the LR_P and SR_G of a P + G structure, respectively. The *dotted curve* stands for the SR_G of a G structure and the *dashed-dotted curve* for the LR_P of a P structure. Real propagation constants of **b** the LR_P and **c** the SR_G plasmon modes as a function of the gold thickness and polar angle. The *solid symbols* correspond to the optically symmetric structure based on an anticrossing bandgap prism coupling technique (PG). The *empty symbols* correspond to the system in which only either a prism (P) or a grating (G) is used. *Squares*, *circles*, *up-triangles*, *down-triangles* and *diamonds* correspond to polar angles of 44.25°, 46.417°, 47.27°, 48° and 49°, respectively

curves would only cross at different polar angles. Therefore, plasmons with the same propagation constant at a fixed gold thickness could only be excited for different polar angles.

The shady region in Fig. 9a corresponds to a collection of propagation constants of LR_P modes supported by a gold grating in our four-mode anticrossing bandgap plasmonic structure. At fixed gold thicknesses, the modes will pass through all values of this area when the polar angle changes from 47.27° to 49°. From that figure, it can be inferred that, for fixed propagation constant, one can choose the right LR_P mode with the deepest plasmon resonance by tuning the t_{Au} and polar angle. This resonance presents a balance between radiation losses and dissipative losses for polar angles that range from 44.25° to 49° [13]. In the same way, one can choose the deepest SR_G, SR_G^G or LR_P^P modes (see Fig. 9b, c).

Therefore, whereas the tuning effect for SR_G modes (Fig. 9c) is pronounced for thinner gold gratings (this is also the case of SPs in Abeles configuration [6]), the tuning effect for LR_P modes is more pronounced for gold gratings thicker than 20 nm (Fig. 9b). Hence, the restriction related to the percolation threshold is not important in the case of LR_P. Nevertheless, we have used for our simulations the safe value of 10 nm as a minimum gold thickness [15, 16].

Note also that in our four-mode anticrossing bandgap plasmonic structure, for a fixed Cytop thickness, the LR_P modes with the same propagation constant at a different wavelength can only be excited for different thicknesses of the metal grating (see Fig. 10). The same assertion is true for SPs at different thicknesses of the bimetallic film in an Abeles configuration [6]. On top of that, our configuration allows changing the propagation constant of the LR_P modes at fixed wavelength by changing the thickness of the gold grating. This gives us the opportunity to find the mode with the deepest LR_P resonance. What is more, this resonance can also be found for a fixed gold thickness by tuning the incident wavelength. Hence, not only in the Abeles configuration is it possible to achieve similar values of the plasmon propagation constant at different wavelengths [6, 17]. For instance, the points marked on Fig. 10b correspond to the same propagation constant of the different LR_P modes obtained for diverse gold thicknesses, but at different wavelengths, in our four-mode anticrossing bandgap configuration.

Therefore, our four-mode plasmonic structure presents several advantages. Up to four different surfaces plasmons can be excited simultaneously at a single location on the sensor, and it can be used in both angular and wavelength interrogation techniques. What is more, the appearance of bandgaps can be useful on different fields as photonics materials or outperforming traditional sensors

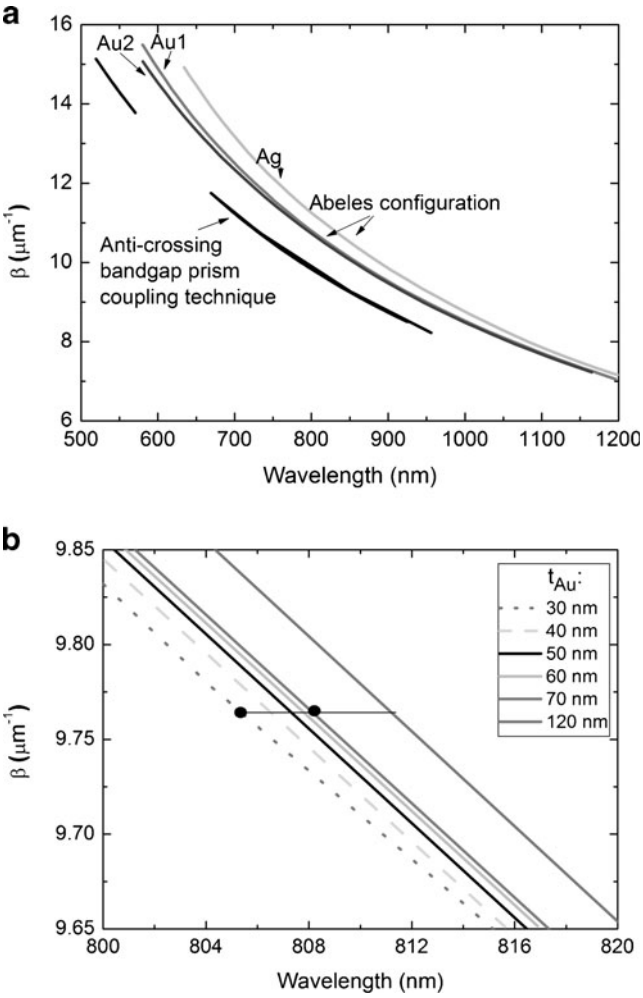

Fig. 10 **a** Propagation constants as a function of λ obtained using the plasmonic structure based on the Abeles configuration in which the metal film consists of silver and gold layers [6, 17]. This is compared to the propagation constant of our plasmonic structure based on an anticrossing bandgap prism coupling technique. **b** Enlargement of **a** to show the influence of the gold thickness on the LR_P propagation constant in our system

due to the increase of the density of the modes on the band edge [18].

Conclusions

We have proposed a novel plasmonic structure based on an anticrossing bandgap prism coupling technique for tuning the propagation constants of long- and short-range surface polaritons by changing the gold thickness of the grating. The prism was used to couple the LRSPPs modes to photons, whereas the grating gives rise to the gap. The good agreement between the experimental and theoretical data supports the validity of our code for this study. The propagation of the different modes (LR_G, SR_G, LR_P and SR_P) is found to be highly dependent on

the gold thickness of the slab. Thus, the variation of λ with t_{Au} in the three regions of the SR_G mode can be described by a potential-type equation: $\lambda/\theta \propto t_{Au}^{b}$, where b informs about the possible coupling. The LR_P mode, on the other hand, was fitted to an exponential decay function and its decay constant $B=104.7/t_{Au}$ suffers an increase of approximately 25 % as a consequence of the coupling between the LR_P and SR_G. These facts allow controlling the distances between branches and the coupling interaction. Moreover, our results have been compared to not only those systems were only the prism or the grating was used but also those systems in Abeles configuration, giving physical insight into the role of each component and the balance between radiation and dumping losses. Our structure provides lower and optimized propagation constants compared to those previously reported [6] and entails a lower attenuation. However, further studies are needed to evaluate the contribution of the different system parameters and increase the sensitivity and resolution of potential plasmonic bio-sensors.

Acknowledgments Financial support by the Max Planck Gesellschaft and the Austrian Institute of Technology (GmbH) is acknowledged. The work was also supported by the EU and the Deutsche Forschungsgemainschaft under projects FP6-2005-FOOD-036300 and KN 224/18-1.

References

1. Okamoto T, Simonen J, Kawata S (2008) Phys Rev B 77:115425
2. Barnes WL, Preist TW, Kitson SC, Sambles JR (1996) Phys Rev B 54:6227
3. Chen Z, Hooper IR, Sambles JR (2008) J Opt A 10:015007
4. Hooper IR, Sambles JR (2004) Phys Rev B 70:045421
5. Sarid D (1981) Phys Rev Lett 47:1927–1930
6. Dyankov G, Zekriti M, Bousmina M (2011) Plasmonics 6:643–650
7. Andreev SN, Belotelov VI, Bykov DA, Doskolovich LL, Tarakanov VP, Zvezdin AK (2011) Opt J Soc Am B 28:1111–1116
8. Ong BH, Yuan X, Tjin SC, Zhang J, Ng HM (2006) Sens Actuators B 114:1028–1034
9. Chuliá-Jordán R, Santamaría-Pérez D (2012) Appl Phys Lett 100:063301
10. Palik ED (1991) Handbook of optical constants of solids. Academic, Boston
11. Maier SA (2007) Plasmonic: fundamentals and applications. Springer, Berlin
12. Rathsfeld A (2009) User guide direct problems for optical gratings over triangular grids. Weierstass-Institut, Berlin
13. Raether H (1988) Surface plasmons on smooth and rough gratings. Springer, Berlin
14. Weber MG, Mills DL (1985) Phys Rev B 32:5057
15. Gompf B, Beister J, Brandt T, Pflaum J, Dressel M (2007) Opt Lett 32:1578–1580
16. Yagil Y, Gadenne P, Julien C, Deutscher G (1992) Phys Rev B 46:2503–2511
17. Abeles F, Lopez-Rios T (1974) Opt Commun 11:89–92
18. Benahmed AJ, Ho C-M (2007) Appl Opt 46:3369–3375